We are IntechOpen, the world's leading publisher of Open Access books Built by scientists, for scientists

4,800
Open access books available

122,000
International authors and editors

135M
Downloads

Our authors are among the

154
Countries delivered to

TOP 1%
most cited scientists

12.2%
Contributors from top 500 universities

WEB OF SCIENCE™

Selection of our books indexed in the Book Citation Index in Web of Science™ Core Collection (BKCI)

Interested in publishing with us?
Contact book.department@intechopen.com

Numbers displayed above are based on latest data collected.
For more information visit www.intechopen.com

14

Strength Prediction of Composite Materials from Nano- to Macro-scale

Konstantinos I. Tserpes
Laboratory of Technology & Strength of Materials, University of Patras
Greece

1. Introduction

The primary scope behind composite materials development was to reduce structural weight and cost. Nowadays, after more than 30 years of development, this scope has been partially achieved through the extensive use of CFRP laminates in aeronautical, automotive and marine applications. During these years, the evolution of composite materials has being mainly accomplished experimentally; the contribution of theoretical modeling although necessary is limited due to the difficulties in stress and failure analyses originating from material complexity. In order to extend the use of composite materials, specific structural problems, such as the increase in out-of-plane strength of laminated composites and effective joining between composite parts, must be resolved. Towards the resolution of these problems, textile composites with 3D reinforcement have been proposed and adhesive bonding is being forwarded as an alternative to mechanical fastening. However, the understanding of the mechanical performance of textile composites is still evolving, while the integrity of adhesively composite bonded joints needs to be improved.

In the last decade, another area has come to the front in the science of composite materials; namely nanocomposites. The spunk for the offset of this area was the discovery of carbon nanotubes and the thereafter findings about their extraordinary mechanical properties. Since then, several works have been reported on the reinforcement of polymers by carbon nanotubes and other nanoparticles. The first findings are very promising; however, there are many issues, such as the strength of the nanotube/polymer interface, the role of nanotube alignment and the structural defects in nanotubes, that must be clarified before nanocomposites are set to production. In the case of nanocomposites, theoretical modeling is more important than in conventional composites since experimenting in the nano-scale is a very tedious task.

It is obvious that theoretical modeling plays a major role in the future developments in the science of composite materials. Among methods used to predict strength of composite materials and structures, progressive damage modeling (PDM) is probably the most adequate since it is capable of simulating the initiation and progression of all damage types in composites and predict strength of the specimen or structure. As the PDM simulates reality, it serves as an ideal complement to experiments because it can be directly compared to any type of experimental result, used for further evaluation of the experimental findings and shed light in damage details which cannot be explained experimentally. In the following, a short historical overview and a description of the method are given.

2. The PDM method

Damage is a multi-scale phenomenon that occurs from the atomic scale (nm) to structural scale (m). It is also of progressive nature as it evolves through the stages of initiation and propagation to catastrophic fracture. Prediction of damage is a diachronic engineering challenge. Most of the models developed for this purpose have been concentrated to one stage; either to damage initiation, thus being unable to predict strength, or to catastrophic fracture, thus neglecting damage history. A progressive damage model takes into account all three stages by predicting damage initiation and progression using failure criteria, simulating the influence of damage presence using material property degradation rules and finally, predicting strength using a final failure criterion. Furthermore, as it simulates the actual phenomenon, it can be implemented, by incorporating the appropriate tools, to engineering problems of any scale ranging from atomic to macroscopic.

The origin of the progressive damage modeling (PDM) method is traced back on 1958 to the damage model of (Kachanov, 1958). However, the onset for the systematic use of the method waited until 1987 when (Chang & Chang, 1987) demonstrated its capability in predicting strength of composite materials. Since then, the method has been evolved rapidly and has found several applications in materials and structures lying in different scales.

The PDM method comprises the modules of *stress analysis*, *failure analysis* and *material property degradation*. These modules integrate in an iterative procedure which is completed as soon as a *final failure criterion* is fulfilled. The iterative procedure in its general form is explained by means of the flowchart shown in Fig.1. In the various applications of the method, many alterations of this flowchart have been adopted. However, the general idea has been kept the same. As the procedure is repeated for each load-level, all data regarding the stress- and strain-field as well as the damage state can be stored and recalled thus, enabling the full description of the component's mechanical behavior.

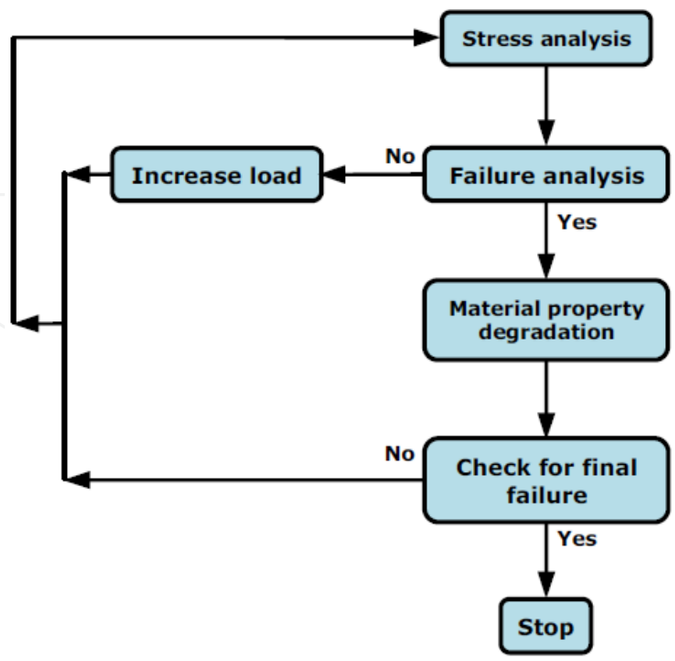

Fig. 1. Flowchart of the PDM method.

3. Summary of the chapter

In this chapter, the capability of the PDM method in predicting strength of composite materials lying in different scales is demonstrated through the description of method's application to 4 different structural problems lying from nano- (nm) to macro-scale (m). The cases considered are schematically described and scaled in Fig.2.

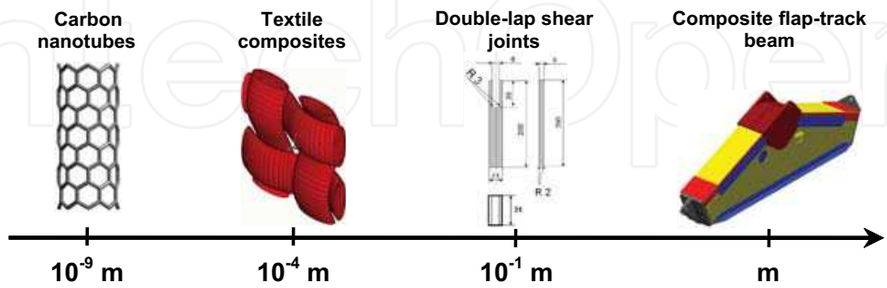

Fig. 2. Schematic description and scaling of the cases in which the PDM method has been applied.

4. Carbon nanotubes

Carbon nanotubes (CNTs) are fullerene-related structures that became public by (Iijima, 1991). They can be visualized as graphene sheets rolled into hollow cylinders composed of hexagonal carbon rings. The nanotube structure is described in terms of a chiral vector defined by the pair of indices (*n*,*m*). According to the values of the indices, three nanotube types arise; namely, the *armchair* (*n*,*n*), the *zigzag* (*n*,0) and the *chiral* (*n*,*m*) CNTs. As the hexagonal pattern is repeated periodically, it leads to binding of each carbon atom to three neighboring atoms via covalent bonds. This covalent bond is one of the strongest chemical bonds in nature. Thus, it was expected to lend impressive mechanical properties to CNTs. Indeed, it has been experimentally and theoretically confirmed by several studies reported in the last decade that carbon nanotubes possess extraordinary mechanical properties (elastic modulus higher than 1 TPa, tensile strength in the range of 150 GPa, elastic strain up to 5% and failure strain up to 20%).

Combining extraordinary mechanical properties and fiber-like structure, CNTs offer unique potential for reinforcing polymers either as replacements of conventional fibers or as fillers to enhance the properties of the existed advanced composites. In (Qian et al., 2002) it has been demonstrated that with only 1% (by weight) of CNTs added in a matrix material, the stiffness of a resulting composite film can increase between 36% and 42% and the tensile strength by 25%. In (Yokozeki et al., 2007) it was observed a clear retardation in matrix cracking onset and accumulation in composite laminates filled with CNTs. Before establishing CNTs as mechanical reinforcements, their mechanical performance needs to be fully understood. At present, since experimentation at the nanoscale is still evolving, the only available tool for accomplishing this task is modeling. To date, two approaches have been mainly adopted: the atomistic and the continuum mechanics approaches. The atomistic simulations are limited in both time and length scales. For example, a 10 nm long single-walled carbon nanotube involves more than 2000 atoms and its atomistic study is computationally intensive. The lack of continuum mechanics models combined with the

limited practical applications of atomistic models necessitates the development of continuum mechanics models able to simulate the mechanical performance of CNTs with large number of atoms under complex mechanical loading conditions, by considering also the topological and/or vacancy defects that may have introduced in the nanotube during its synthesis process. In (Tserpes & Papanikos, 2006), an atomistic-based progressive fracture model, which fulfills these requirements, was developed. The model will be described in the following sections.

4.1 A progressive fracture model for CNTs

The progressive fracture model is an atomistic-based continuum approach as it uses the FE method to analyze the structure of CNTs and an interatomic potential to describe the non-linear behavior of the C-C bonds. In the model, CNTs are treated as space-frame structures (Tserpes & Papanikos, 2005). As the FE model was developed using the ANSYS FE code, the model was entirely implemented using the ANSYS APDL macro-language.

4.1.1 Simulation of non-linear behavior of the C-C bonds

For simulating the non-linear behavior, the pairwise modified Morse potential (Belytschko et al., 2002) was used. This decision was strongly enforced by the simplicity of the specific potential over many-body potentials. To date, the modified Morse potential has been adequately applied in a number of cases where there are large deviations from equilibrium due to the presence of large strains.

According to the modified Morse potential, the potential energy of the nanotube system is expressed as

$$E = E_{stretch} + E_{angle}\,, \tag{1}$$

$$E_{stretch} = D_e\{1 - e^{-\beta(r-r_0)}]^2 - 1\}\,, \tag{2}$$

$$E_{angle} = \frac{1}{2}k_\theta(\theta-\theta_0)^2[1 + k_{sextic}(\theta-\theta_0)^4]\,, \tag{3}$$

where $E_{stretch}$ is the bond energy due to bond stretching and E_{angle} the bond energy due to bond angle-bending, r is the current bond length and θ is the current angle of the adjacent bond. The parameters of the potential are:

$$r_0 = 1.421\times10^{-10}\,m\,,\ D_e = 6.03105\times10^{-19}\,Nm\,,\ \beta = 2.625\times10^{10}\,m^{-1}\,,\ \theta_0 = 2.094\,rad\,,$$
$$k_\theta = 0.9\times10^{-18}\,Nm/rad^2\,,\ k_{sextic} = 0.754\,rad^{-4}\,.$$

As bond stretching dominates nanotube fracture and the effect of angle-bending potential is very small, only the bond stretching potential has been considered.

By differentiating Eq.(2), the stretching force of atomic bonds is obtained in the molecular force-field as

$$F = 2\beta D_e(1 - e^{\beta(r-r_0)})e^{-\beta(r-r_0)} \tag{4}$$

Fig.3 plots the relationship between force F and bond strain ε for the C-C bonds. The strain of the bond is defined by $\varepsilon = (r - r_0)/r_0$. As may be seen, the force-strain relation is highly

non-linear at the attraction region especially at large strains. The inflection point (peak force) occurs at 19% strain. The repulsive force $(\varepsilon < 0)$ increases rapidly as the bond length shortens from the equilibrium length with less non-linearity than the attractive force.

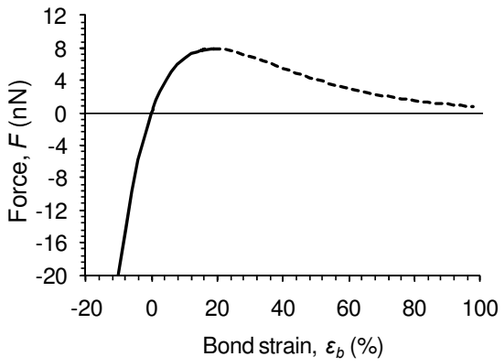

Fig. 3. Force-strain curve of the modified Morse potential.

4.1.2 Model algorithm

For modeling the C-C bonds, the 3D elastic ANSYS BEAM4 element was used. The non-linear behavior of the C-C bonds, as described by the interatomic potential, was assigned to the beam elements using the stepwise procedure of progressive fracture modeling, which is briefly described in the following lines. Initially, the stiffness of the beam elements is evaluated from the initial slope of the force-strain curve of the modified Morse potential (Fig.3) using the element's cross-sectional area A. The initial stiffness is 1.16 TPa. The nanotube is loaded by an incremental displacement at one of each ends with the other end being fully constrained. Zero transverse displacement was applied to the loading end in order to prevent buckling of nanotube at high loads. Fig.4 shows the FE mesh of the (20,0) nanotube along with the applied boundary conditions. At each load step, the stiffness of each element is set equal to $F/A\varepsilon$, where ε is the axial strain of the element as evaluated from the FE model and F is the interatomic force calculated using Eq.(4). This calculation of stiffness is applied until the inflection strain of the interatomic potential. When the axial strain of a bond reaches the inflection strain (19%) its stiffness is suddenly degraded (10^{-6} of the initial value) and the bond is disabled from carrying load. The next displacement increment is then applied to the nanotube and this iterative procedure goes on until catastrophic failure of the nanotube takes place.

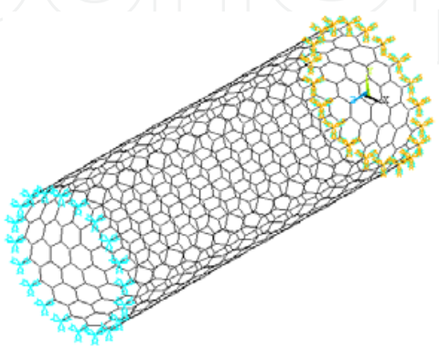

Fig. 4. FE mesh and boundary conditions of the (20,0) nanotube under axial tension.

4.2 Tensile behavior of pristine and defected CNTs

The progressive fracture model has been applied to simulate the tensile behavior of the zigzag (20,0) nanotube containing a defect of 10% weakening of one bond and a vacancy defect (1 missing atom). Numerical predictions are compared with the experimental measurements of (Yu et al., 2000) and the molecular mechanics simulations of (Belytschko et al., 2002). Fig.5 shows the comparison between the stress-strain curves. In (Yu et al., 2002) several experiments have been performed. The measured stress-strain curves show very large dispersion. As the comparison with the whole number of the curves would be valueless, three of those, which show the best correlation, have included in Fig.5. Curves that concern both types of initial defects are displayed. As may be seen, both theoretical models significantly overestimate the Young's modulus and strength of CNTs. The most possible cause for this discrepancy is the defects of unknown type and amount that appear in the nanotubes tested by (Yu et al., 2000) and not considered by the two models. In (Mielke et al., 2004) it was found that large approximately circular holes, which would be consistent with damage resulting from harsh oxidative purification processes, may substantially reduce the failure stresses and failure strains of CNTs, providing a likely explanation for the discrepancy. Specifically, in (Mielke et al., 2004) it was found that the one- and two-atom vacancy defects reduced the failure stresses by as much as 26% approaching thus the experimental failure stresses. Another possible cause, as stated in (Belytschko et al., 2002), is the slippage that possibly occurred at the attachments for the high strain cases reported in (Yu et al., 2000) resulting in a decrease of the measured values of nanotube Young's modulus. This kind of slippage would also imply that the failure strains are actually smaller than reported.

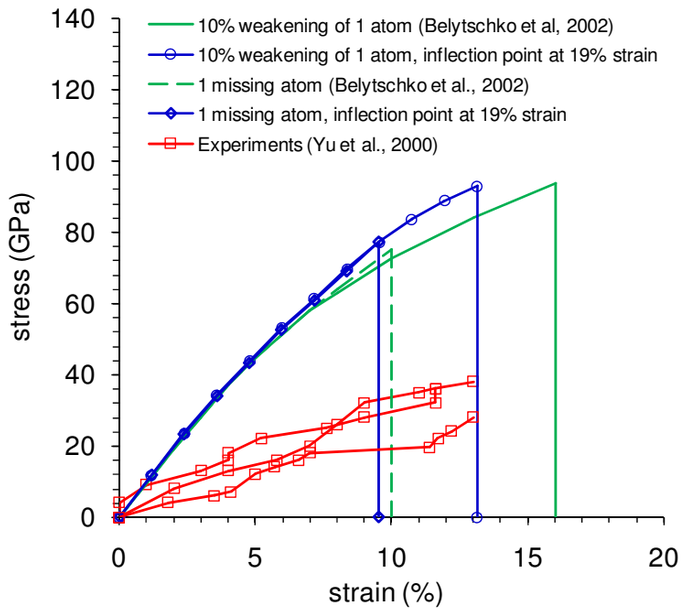

Fig. 5. Comparison between predicted tensile stress-strain curves with experimental and theoretical curves obtained from the literature.

Concerning the comparison between the progressive fracture model and the simulations of (Belytschko et al., 2002), a very good agreement is achieved regarding the Young's modulus and tensile strength of the nanotubes. The curves obtained by the two methods for both

types of initial defects coincide up to 8% strain giving the same Young's modulus for the nanotubes. For strains larger than 8%, the model predicts higher Young's modulus than the molecular mechanics simulations. Nevertheless, the fracture strain predicted by the model in this case (13.12%) was equal to the one obtained by two different experiments of (Yu et al., 2000).

Fig.6 shows the evolution of fracture as function of nanotube elongation in the (20,0) tube, in which the vacancy defect was modeled. As may be seen, in this case, fracture propagated circumferentially at the same row of bonds without any spreading until fracture of all bonds around circumference (separation of nanotube). The same evolution of fracture has been also obtained by (Belytschko et al., 2002) for the same nanotube and initial defect.

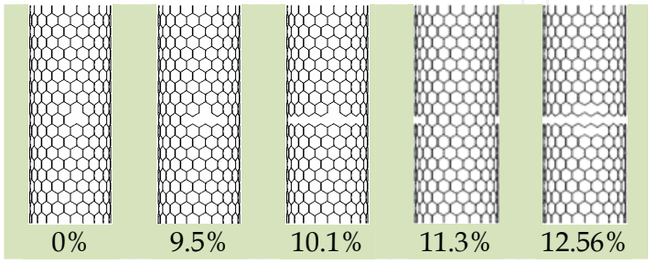

Fig. 6. Predicted evolution of fracture at the (20,0) nanotube as a function of applied strain.

The progressive fracture model described in this section is in advantage over classical atomistic approaches, such as molecular mechanics, in the sense that is simpler and performs in much smaller CPU times. All the analyses conducted within the frame of the current work took less than 1 minute in a Pentium 4 CPU 3.2 GHz, 1.0 GB RAM personal computer. Consequently, the model can be applied in CNT systems with very large number of atoms where the use of molecular mechanics simulations is unpractical. Moreover, the adoption of the FE method gives the model the potentiality to also simulate CNT-based nanostructures.

5. Textile composites

Textile composites, especially those with 3D reinforcement, offer enhanced through-thickness performance which is the weak point of laminated composites. Understanding of the mechanical behavior of textile composites is in progress. Both experimental and theoretical tools are being adopted. Modeling of textile composites is a very tedious task due to their complicated micro-geometry. Existing numerical tools and analytical relations, as have been developed for unidirectional laminates, are inapplicable. For instance, the widely used layered elements available in commercial FE codes cannot be used for the stress analysis of textile composites. Multi-scale approaches, that are capable to efficiently transfer the material's behavior from the micro- to the macro-scale, offer a base for facing this demanding modeling task. Several works have been reported on the modeling of textile composites. Most of them are based on a representative volume element (RVE) homogenized using finite elements to derive the mechanical properties of the textile composite material. Only few works have considered failure initiation and progression in order to evaluate the mechanical response of the material. Therefore, there is still a need for modeling the mechanical response of textile composites based on simulations of failure behavior. The most proper way to accomplish this is homogenized PDM incorporating the

appropriate tools. In (Tserpes & Labeas, 2010) a multi-scale PDM was used to simulate the mechanical response of plain weave composites and cellular solids. In this section, the first part of this work concerning plain weave composites will be summarized.

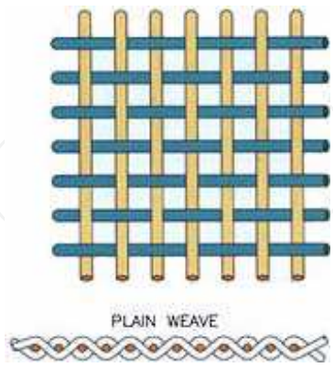

Fig. 7. Schematic of the plain weave composite material.

5.1 The multi-scale damage model

The flowchart of the multi-scale damage model is shown in Fig.8. The basic characteristic of the model is the proper definition of the RVE both in terms of geometry and size. Innovation of the model is the performance of homogenized PDM using up-to-date theoretical tools that ensures the accurate simulation of the mechanical response of the material system. In the following, the adjustment of each model component to the two material systems is described.

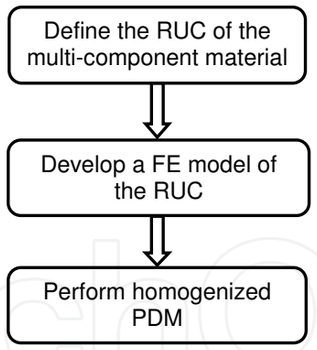

Fig. 8. Flowchart of the multi-scale damage model.

5.1.1 Development of the RVE

The RVE of the plain weave material system is defined as a rectangular volume containing two fill and two warp tows, with a length being representative of the crimp between them, and the surrounding matrix. The geometry of the RVE, taken from (Tang & Whitcomb, 2003) to enable comparison, was created using the software package WiseTex (Verpoest & Lomov, 2005) which possess specific capabilities in the creation of the micro-geometry of textile composite materials. The software requires as input the number of fill and warp tows, the crimp function and the geometry of the cross-sectional area of the tows. The RVE of the plain weave material is schematically described in Fig.9.

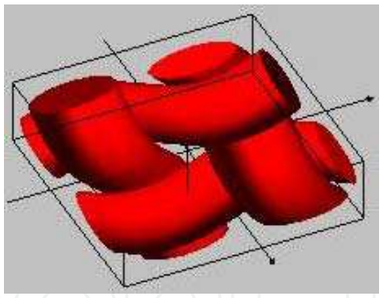

Fig. 9. Schematic representation of the plain weave's RVE.

5.1.2 FE modeling of the RVE

Creation of the FE model of the RVE was done by means of a semi-automated procedure: volumes, areas and lines were initially automatically generated in the ANSYS code by importing the RVE geometry of the RVE from WiseTex (Verpoest & Lomov, 2005) and the FE mesh of the RVE was generated manually in order to achieve compatibility between the different parts. Due to mesh compatibility, the coincident nodes of different parts were merged, thus implying a fully bonded structure. All parts have been modeled using the 3D 8-noded SOLID185 element which is appropriate for 3D modeling of solid structures. Typical FE meshes of the RVE and fiber tows are shown in Fig.10. Loading conditions and periodic boundary conditions have been also applied through the WiseTex software by means of a separate input file. This procedure requires as input the direction and magnitude of the applied strain and the software generates automatically the periodic boundary conditions for the specific load-case. In the present application, an incremental axial strain was applied to simulate axial tension of the plain weave.

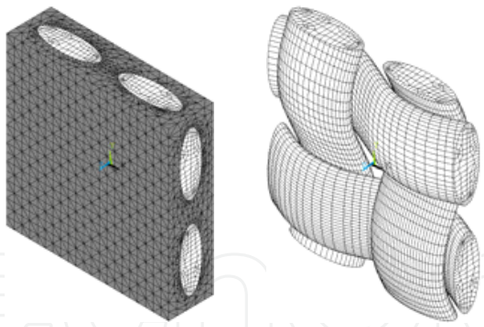

a b

Fig. 10. FE mesh of a. the full RVE of the plain weave, and b. the tows.

5.1.3 Damage analysis

Failure analysis of textile composites is a tedious task since the available failure theories have been developed for unidirectional laminates. However, it has been shown recently that the Hashin-type polynomial failure criteria give in some cases accurate predictions for textile composites also. In (Tserpes & Labeas, 2007) the stress-based Hashin-type failure criteria have been successfully applied to simulate the tensile behavior of non-crimp fabric composites, while in (Xiao et al., 2007) the strain-based Hashin-type failure criteria have been used to simulate progressive damage and delamination in PW S-2 glass/SC-15

composites under quasi-static punch-shear loading. In the present work, the strain-based criteria were used as they fit well with the damage mechanics approach used to imply material property degradation.

For the tows, four different failure modes have been considered; namely: fiber tensile/shear failure, matrix cracking/shear failure, fiber compressive failure, matrix compressive failure, fiber in-plane shear failure and delamination failure. The failure criteria for the detection the failure modes are described in the following

Fiber tensile/shear failure:

$$r_1^2 = \left(\frac{E_f \varepsilon_f}{S_{ft}}\right)^2 + \left(\frac{G_{fn}\varepsilon_{fn}}{S_{fn}}\right)^2 \quad (f\text{-direction}) \tag{5}$$

Matrix cracking/shear failure:

$$r_2^2 = \left(\frac{E_w \varepsilon_w}{S_{wt}}\right)^2 + \left(\frac{G_{wn}\varepsilon_{wn}}{S_{wn}}\right)^2 \quad (w\text{-direction}) \tag{6}$$

where f, n denotes the in-plane fill and out-of-plane directions, respectively. t, s denote the tensile and shear strengths, respectively. E and G are the axial and shear elastic moduli, respectively, while ε is the tensile strain. S_{ft} and S_{wt} are the tensile strengths in the fill and warp directions, respectively, while S_{fn} and S_{wn} the shear failure strengths in the fn and wn planes, respectively.

Fiber compressive failure:

$$r_3^2 = \left(\frac{E_f \cdot \varepsilon'_f}{S_{fc}}\right)^2, \varepsilon'_f = -\varepsilon_f - \langle \varepsilon_n \rangle \frac{E_n}{E_f} \quad (f\text{-direction}) \tag{7}$$

Matrix compressive failure:

$$r_4^2 = \left(\frac{E_w \cdot \varepsilon'_w}{S_{wc}}\right)^2, \varepsilon'_w = -\varepsilon_w - \langle \varepsilon_n \rangle \frac{E_n}{E_w}, \quad (w\text{-direction}) \tag{8}$$

where S_{fc} and S_{wc} are the compressive strengths in the fill and warp directions, respectively.

Fiber in-plane shear failure:

$$r_5^2 = \left(\frac{G_{fw} \cdot \varepsilon_{fw}}{S_{fw}}\right)^2 \tag{9}$$

where S_{fw} is the tow shear strength due to matrix shear failure.

Delamination:

$$r_6^2 = S^2 \left[\left(\frac{E_n \cdot \varepsilon_n}{S_{nt}}\right)^2 + \left(\frac{G_{wn} \cdot \varepsilon_{wn}}{S_{wn0}}\right)^2 + \left(\frac{G_{nf} \cdot \varepsilon_{nf}}{S_{fn0}}\right)^2 \right] \tag{10}$$

where S_{nt} is the through-thickness tensile strength, S_{wn0} and S_{fn0} are the interlaminar shear strengths in *wn* and *fn* planes, respectively and *S* is a factor to take into account stress concentration on the growth of delamination equals to 1.2.

It is well known that textile composites and especially the PW possess a non-linear behavior due to matrix cracking and shear failures that appear at resin-rich pockets and tows. As these failure modes result from complex stress states, in order to predict them failure criteria that incorporate coupling between different stresses must be adopted. Such criteria are those described above. Along with failure criteria, a gradual material property degradation concept must be applied. Such a concept is the damage mechanics concept of (Matzenmiller et al., 1995) that incorporates also features for controlling strain softening. Note that the specific combination of the failure criteria and material property degradation has been used successfully in (Xiao et al., 2007). According to the damage mechanics concept, the presence of damage is simulated by the reduction of stiffness based on the functions

$$E_i = (1-\omega_i)E_{i0},\ G_i = (1-\omega_i)G_{i0} \tag{11}$$

where E_{i0} and G_{i0} are the initial values of the moduli and ω_i is the damage variable given by

$$\omega_i = \max\{q_{ij}\phi_j\},\ j = 1,...,6 \tag{12}$$

$$\phi_i = 1 - e^{\frac{1}{m}(1-r_j^m)},\ r_j \geq 1 \tag{13}$$

where r_j is the failure index derived from Eq.(5), *m* is the softening parameter equals to 2 and q_{ij} is the vector-value function indicating coupling between damage variables and damage modes $(j = 1,...,6)$ described in the following table

$$[q] = \begin{bmatrix} 1 & 1 & 1 & 0 & 0 \\ 0 & 0 & 1 & 0 & 0 \\ 0 & 0 & 1 & 0 & 1 \\ 1 & 1 & 1 & 1 & 1 \\ 0 & 0 & 1 & 0 & 0 \\ 1 & 1 & 1 & 0 & 1 \end{bmatrix} \tag{14}$$

Combining Eqs.(8) and (10) we get

$$\begin{aligned} \omega_1 &= \max\{\phi_1, \phi_2, \phi_3\} \\ \omega_2 &= \phi_3 \\ \omega_3 &= \max\{\phi_3, \phi_5\} \\ \omega_4 &= \max\{\phi_1, \phi_2, \phi_3, \phi_4, \phi_5\} \\ \omega_5 = \phi_3 \ \ \omega_6 &= \max\{\phi_1, \phi_2, \phi_3, \phi_5\} \end{aligned} \tag{15}$$

The damage variables apply with the above order to $E_f, E_w, E_n, G_{fn}, G_{wn}$ and G_{fn}, respectively.

The modules of stress analysis, failure analysis and material property degradation are integrated in an iterative algorithm. To demonstrate the algorithm, consider the fiber

tensile/shear failure in fill direction. From the stress analysis the strains are derived for each element. Then, parameter r_1 is derived from failure criterion of Eq.(7), ϕ_1 , ϕ_2 and ϕ_3 from Eq.(12) and ω_1 from Eq.(15) to finally evaluate the degraded value of E_f from Eq.(11).
For the epoxy resin, the Maximum Stress failure criterion was used to check for possible failures in all material directions. Whenever a stress exceeded strength, the stiffness in the respective material direction was totally degraded.

5.2 Tensile response of plain weave composites

A study on the effect of degradation factor m on the predicted tensile response of the PW was conducted. Fig.11 compares the predicted tensile stress-strain curves for the cases of m =0.001, m =2 and m =8 with the curve predicted by (Tang and Whitcomb, 2003) using the maximum stress failure criterion and sudden material property degradation rules. The different degradation concepts are explained in Fig.12 by means of the resulted tensile stress-strain curves. The simple sudden degradation concept implies a constant Young's modulus until failure is predicted by the failure criterion. Then, the Young's modulus drops to a very small value, thus implying a continuously increasing strain with a constant stress. On the other hand, the damage mechanics concept of (Matzenmiller et al., 1995) implies a non-linear behavior from the first stages of loading as the Young's modulus decreases with increasing strain until a large drop to take place at a certain strain threshold. From that point and on the material behavior is governed by the degradation factor. For very small values of m (e.g. 0.001), the concept tends to coincide with the sudden degradation concept. With increasing m, a softening part appears. The softening rate increases with increasing m. The difference in the degradation concepts, in terms of the predicted tensile response of the plain weave material, is descriptively illustrated in Fig.8. The sudden degradation concepts give a bilinear behavior of the plain weave material. Transition between the two linear regimes is due to the accumulation of matrix cracking in the matrix and warp tows. The most significant finding is the large deviation in the predicted maximum load between the sudden degradation concepts and the damage mechanics concept. The deviation between the prediction of (Tang & Whitcomb, 2003) and the present prediction taken with m =0.001 is attributed to the different failure criteria used. In the case of the damage mechanics concept, the use of m =8 led to a more degraded behavior of the material compared to m =2 especially at large strains.
A physical interpretation can be given to the damage mechanics concept by relating the degradation in material's behavior with the damage mechanisms. Matrix cracking in warp tows as well as fiber in-plane shear failure initiate at the very early stages of loading and continue to accumulate until final failure to occur. Those failures are responsible for the non-linear behavior of the material. Final failure, considered to take place at maximum sustained load, is due to fiber tensile/shear failure in fill tows initiated at the areas of maximum curvature where longitudinal strain maximizes (see Fig.13). At this point, a small amount of delamination is also predicted to occur mainly at specimen edges attributed to stress redistribution caused by the accumulation of the aforementioned failure modes.
To conclude the present section, a non-linear tensile response, governed by matrix cracking at the resin-rich areas and warp tows, is predicted for the plain weave material. Final failure is due to fiber tensile failure in the fill tows. The comparison between the damage mechanics concept and the sudden degradation concept showed significant deviations mainly at the predicted maximum load. Due to the non-linear response of the material, the damage

mechanics concept is more appropriate as it incorporates features for controlling material softening. However, the proper use of the concept requires calibration of the degradation factor based on experiments.

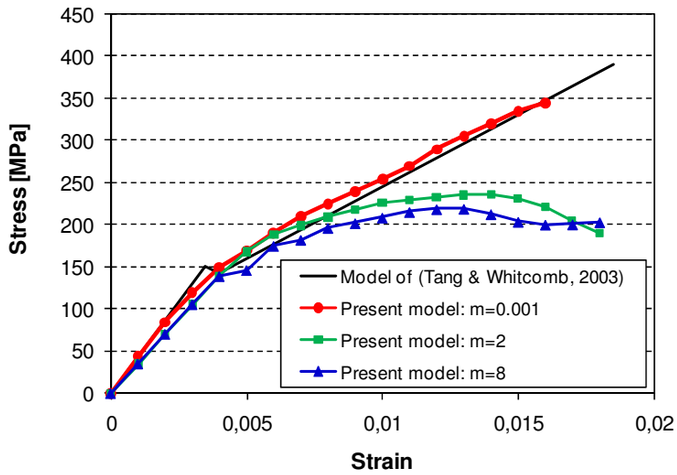

Fig. 11. Comparison of the predicted tensile stress-strain curves of the plain weave material obtained using m =0.001, m =2 and m =8 with the curve obtained in (Tang & Whitcomb, 2003) using the maximum stress failure criterion and the sudden degradation concept.

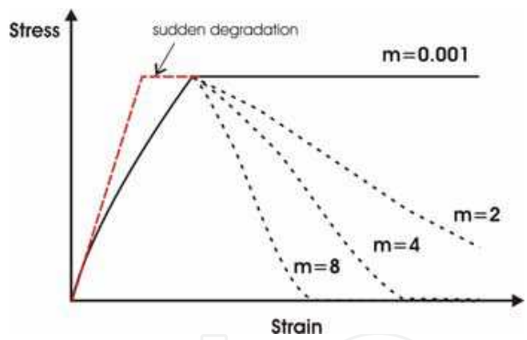

Fig. 12. Illustration of the different degradation concepts.

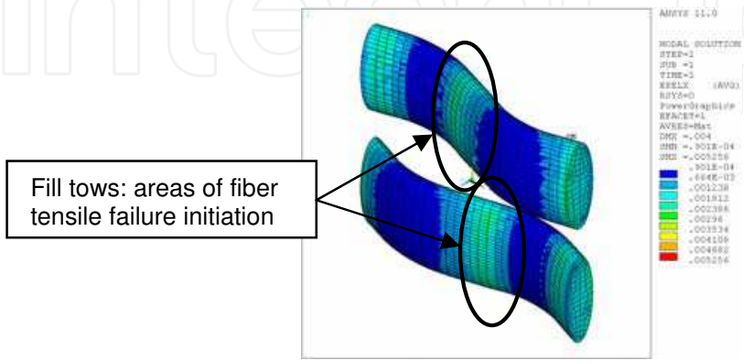

Fig. 13. Contour of longitudinal strain in fill tows and indication of fiber tensile failure initiation.

6. Double-lap shear joint

Currently in aerostructures carbon-fiber reinforced plastics are being mainly assembled by mechanical fasteners. This type of design implies weight penalties emanating from the need to deal with the stress concentrations developed around the bolts. Adhesive bonding serves as the most compatible alternative joining method for composite structural parts providing significant cost and weight savings. For establishing adhesive bonding as a reliable joining method, the ability of bonded joints to efficiently transfer load between assembled parts must be fully ensured. This pertains equally to the integrity of the joining element and bondline. As bonded joints are designed such that the load is transferred through shear, normal tensile loads arise in specific areas of the composite joining element. In bonded joints between traditional composite laminates such loads may lead to delamination in either the joining element or the assembled parts. Therefore, for this kind of applications, new composite materials with enhanced through thickness properties must be employed. Such materials are the 2D and 3D woven fabrics and the non-crimp fabric (NCF) composites.
In (Llopart et al., 2010) several aspects of adhesive bonding technology mentioned in this paragraph have been addressed by using the mesomechanical model developed in (Tserpes & Labeas, 2009) to study the influence of imperfect bonding, in terms of partial lack of adhesion, on the tensile strength of NCF Pi-shaped double-lap shear adhesively bonded joint schematically described in Fig.14. Manufacturing of the NCF joint elements and bonding between the assembled parts were carried out using novel techniques. Quality of adhesive bonding was tested using ultrasonic C-scan inspection.

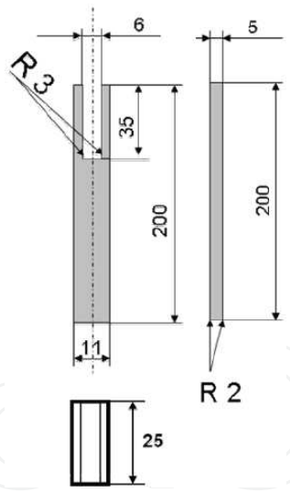

Fig. 14. Schematic representation of the NCF Pi-shaped DLS joint.

6.1 The mesomechanical model

A general description of the mesomechanical model is given by means of the flowchart shown in Fig.15. In brief, the model comprises the steps of:

- definition of the RVE of the woven fabric composite,
- characterization of the mechanical behavior of the RVE using local homogenized PDM,
- development of the FE model of the joint,
- assignment of the behavior of the RVE to the elements of the FE model and implementation of PDM to simulate the global mechanical performance of the joint.

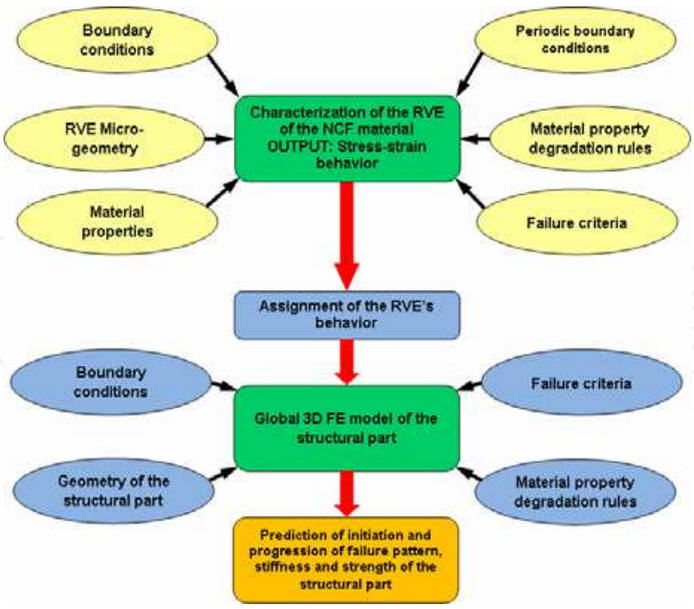

Fig. 15. The flowchart of the mesomechanical model.

6.1.1 Characterization of the mechanical behavior of the RVEs

The DSL joint comprises a combination of the dual layers $0^\circ/90^\circ$, $90^\circ/0^\circ$, $45^\circ/135^\circ$, $135^\circ/45^\circ$ and the unidirectional mono-layers 0°. A schematic description of the joint's lay-up is shown in Fig.16(a). The first two modules of the model concern the material characterization of these NCF HTS/RTM6 material system. For these dual layers, suitable RVEs have been defined in (Tserpes & Labeas, 2009). The result of this characterization is the stress-strain behavior of the two dual layers and summarized in Tables 1 and 2, respectively.

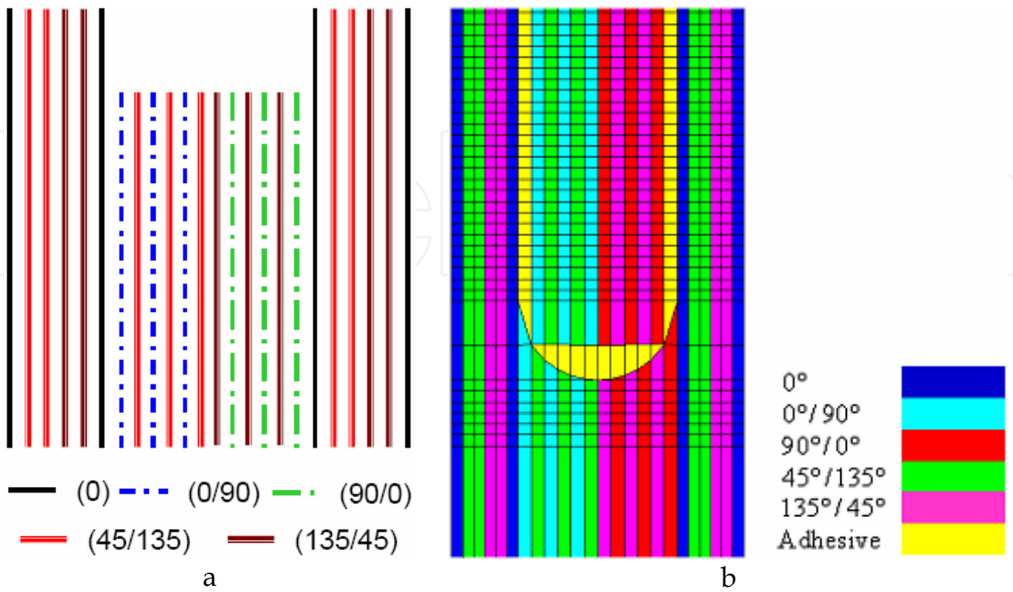

Fig. 16.a. Schematic description of the lay-up and b. Front-view of the FE mesh of the DLS joint.

	Simulated behavior of dual layer $0^\circ/90^\circ$	
Load- case	**Stiffness (MPa)**	**Strength (MPa)**
Longitudinal tension	$E_1^T = -6E+10\varepsilon_1^3 + 7E+08\varepsilon_1^2 - 3+06\varepsilon_1 + 75859$	$S_1^T = 629$
Longitudinal compression	$E_1^C = 76474$	$S_1^C = 764$
Transverse tension	$E_2^T = -595543\varepsilon_2 + 72379$	$S_2^T = 820$
Transverse compression	$E_2^C = 70413$	$S_2^C = 766$
Normal tension	$E_3^T = 11398$	$S_3^T = 74$
Normal compression	$E_3^C = 11398$	$S_3^C = 262$
In-plane shear	$G_{12} = 4250$	$S_{12} = 47$
Out-of-plane shear, *XZ*	$G_{13} = 4270$	$S_{13} = 47$
Out-of-plane shear, *YZ*	$G_{23} = 4290$	$S_{23} = 47$

Table 1. Numerically characterized behavior of the NCF HTS/RTM6 $0^\circ/90^\circ$ dual layer.

	Simulated behavior of dual layer $45^\circ/135^\circ$	
Load- case	**Stiffness (MPa)**	**Strength (MPa)**
Longitudinal tension	$E_1^T = 3E+10\varepsilon_1^3 - 5E+08\varepsilon_1^2 + 571209\varepsilon_1 + 22434$	$S_1^T = 111.4$
Longitudinal compression	$E_1^C = -1E+09\varepsilon_1^2 - 3E+06\varepsilon_1 + 19090$	$S_1^C = 48$
Transverse tension	$E_2^T = -9E+07\varepsilon_2^2 - 209462\varepsilon_2 + 21475$	$S_2^T = 117$
Transverse compression	$E_2^C = -2E+08\varepsilon_2^2 + 1E+06\varepsilon_2 + 20256$	$S_2^C = 145$
Normal tension	$E_3^T = 11398$	$S_3^T = 74$
Normal compression	$E_3^C = 11398$	$S_3^C = 278$
In-plane shear	$G_{12} = -7E+08\gamma_{12}^2 + 155230\gamma_{12} + 24864$	$S_{12} = 41$
Out-of-plane shear, *XZ*	$G_{13} = 4200$	$S_{13} = 46.5$
Out-of-plane shear, *YZ*	$G_{23} = 4261$	$S_{23} = 47$

Table 2. Numerically characterized behavior of the NCF HTS/RTM6 $45^\circ/135^\circ$ dual layer.

Index 1 refers to the direction of fibers, 2 to the transverse direction (matrix) and 3 to the normal direction. Index *T* refers to tensile and *C* to compressive.

6.1.2 FE modeling of the DLS joint

A 3D FE model of the DLS joint was constructed using the commercial FE code ANSYS. All parts were modeled using the structural solid SOLID45 element. Each of the composite biaxial layers was represented by a single row of elements. At each element, the behavior of the corresponding RVE described in Tables 2 and 3 was assigned. Fig.16 shows the correspondence between the dual layers and the element rows. At the elements with lay-up $135^\circ/45^\circ$ and $90^\circ/0^\circ$, the behaviors of the $45^\circ/135^\circ$ and $0^\circ/90^\circ$ RVEs were assigned, respectively. For the UD layer, the elastic properties and strengths of the unidirectional HTS/RTM6 lamina were used. A linear behavior up to failure was assumed for the UD layer.

In order to control and assure that the adhesive has spread out to the full surface on both sides of the insert/Pi-walls interface, non destructive tests (NDT) were carried out on the bonded specimens by means of ultrasonic C-scan. In order to quantify the lack of adhesive, the Imperfect Bonding Severity (IBS) ratio, equals to the total area without adhesive over the desired side bonded area (35 x 250 mm^2), is defined. The IBS ratio was automatically derived for each bonded plate using the statistic function of C-scan analysis.

Fig.17 shows the C-scan images of the DLS specimens for the three sets of tests. The two C-scan images correspond to the two sides of the Pi joint. The meaning of the different colors is explained in the figure. These sets were chosen because they are of representative imperfect bonding severity. As indicated by the values of the IBS ratio, sets 1, 2 and 3 comprise cases of medium, large and small severity, respectively. After NDT inspection, six specimens were cut out from each bonded plate.

Three different cases of imperfect bonding were modeled, namely C1, C2 and C3, being representative of the C-scan findings shown on Fig.17. Case C1 corresponds to the ideal situation (IBS=0% at both sides), case C2 corresponds to set 1 and case C3 to set 2. Lack of adhesive was simulated by subtracting from the FE model the elements of the adhesive included in the misbonded areas. Fig.18 shows the FE meshes of the adhesive for the three modeled cases. In C2 case, at one side of the joint 22% of the adhesive was subtracted. Likewise, in C3, 18% and 81% of the adhesive were subtracted from the two sides of the joint, respectively.

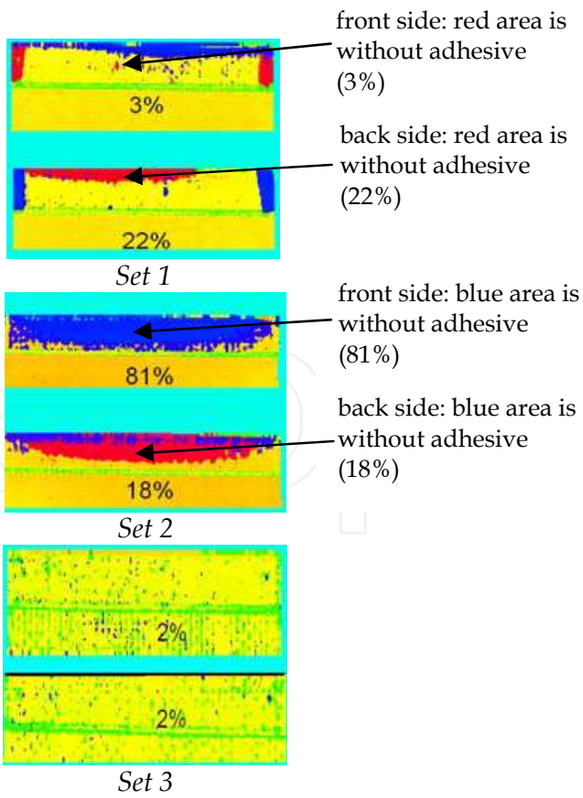

Fig. 17. C-scan images of the specimens indicating the amount of imperfect bonding.

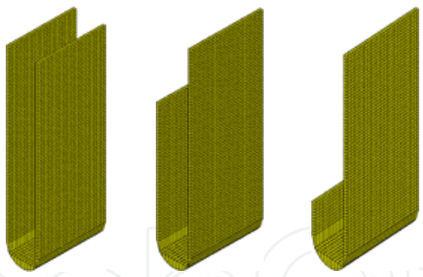

Fig. 18. FE meshes of the adhesives for the three cases modeled.

6.1.3 Damage analysis

At each load step, failure analysis and material property degradation are performed consecutively both at the NCF material (Pi-profile and insert) and the adhesive. Element failures are predicted by comparing stresses with material strengths at each direction (Maximum Stress failure criterion). As soon as failure is reached, the stiffnesses of the failed elements are degraded according to the severity of the failure. Failure in the fibers direction is assumed to be catastrophic and thus, all stiffnesses are degraded in order to totally disable the elements from carrying load. On the contrary, when failure is predicted in the directions transverse and normal to the fibers, the corresponding stiffnesses are degraded such as to disable the load-carrying capability only at the specific directions. Details about the material property degradation rules can be found in (Llopart et al., 2010) Prediction of debonding is fundamental since it is expected to be the primary failure mode of the DLS joint. Debonding is mainly due to shear failure of the adhesive between the Pi-flanges and insert caused by large shear stresses. Secondary debonding may occur due to tensile fracture owing to large normal tensile axial stresses developed between insert's head and Pi-slot. The afore-mentioned failures are respectively predicted using the following two criteria

$$\tau_{\max} = \frac{\sigma_1 - \sigma_3}{2} \geq \tau_a \tag{16}$$

$$\sigma_y \geq S^T \tag{17}$$

where $\tau_{\max}$ is the maximum shear stress at the adhesive, σ_1, σ_3 are the maximum and minimum principal stresses, respectively, and σ_y is the normal axial stress at the loading direction. As soon as failure is predicted in an element of the adhesive, its stiffness is totally degraded to simulate debonding. Plasticity of the adhesive has not been taken into account.

6.2 Numerical results

Fig.19(a) compares the predicted force-displacement curves for the three cases modeled. The curves have been plotted up to the maximum sustained force, which as in the experiments is set to be the strength of the specimen. Comparison reveals that the lack of adhesive causes a small decrease in the stiffness of the specimen and a dramatic decrease in strength. For the effect in strength to be clearer, predicted strengths along with the average experimental strengths of sets 1 and 2 are shown together in Fig.19(b). Set 3 has been excluded from the

comparison due to the reasons discussed in section 4.1. Predicted strengths of imperfect bonded specimens C2 and C3 are degraded by 6.25 and 43.75%, respectively, with regard to the strength of the perfectly bonded C1 specimen. Similarly, the average experimental strength of set 2 specimens is degraded by 29.6% with regard to the strength of set 1 specimens.

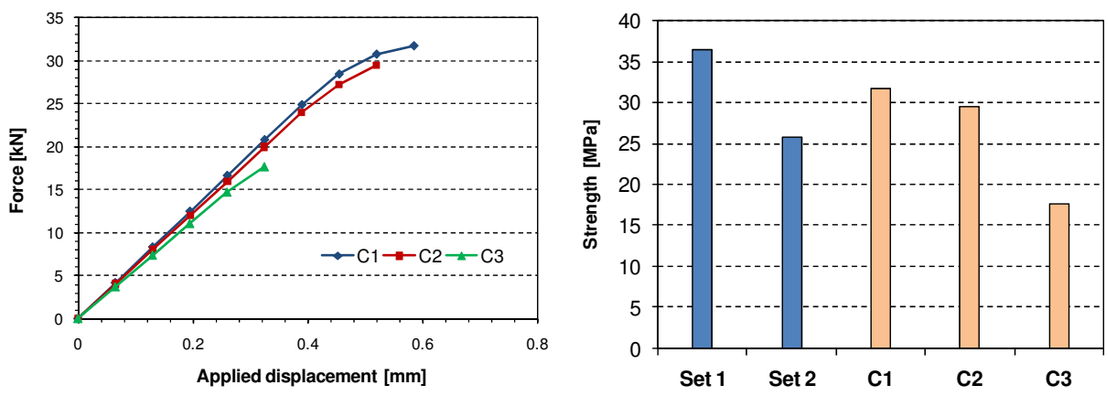

a b

Fig. 19. a. The predicted force-displacement curves of the DLS joints, and b. Experimental and numerical failure loads of the DLS joints.

Due to its progressive nature, the model has the capability of simulating the failure initiation and progression at the NCF material and the adhesive. In the C1 specimen, shear failure of the adhesive (debonding) and transverse tensile failure (matrix cracking) of the UD composite layer are the primary failure modes predicted. Debonding initiated almost simultaneously at the area between insert's head and Pi-slot and at the upper edge of the adhesive where the respective stresses maximize. As the load increases, debonding propagated towards the center of the bonded area. Above a certain load level, propagation of debonding from the lower edge is due to shear stress. Initiation and progression of debonding as a function of pull-out force for the C1 case are illustrated in Fig.20a. Soon after debonding initiated, matrix cracking did so at the UD composite boundary layer as illustrated in Fig.20b. Specimen failed when more than half of the bonded area was debonded. At this point, matrix cracking had accumulated at almost half of the UD composite boundary layer. In C2 specimen, the same failure events with C1 took place with the difference that matrix cracking accumulated in much less degree at the UD composite layer. In C3 specimen, failure is due to adhesive shear failure and no other failures were predicted. Lack of adhesive at the imperfect bonded specimens causes the development of stress concentrations, since the same force is being transferred by less adhesive, which lead to early initiation and fast progression of adhesive shear failure. Thus, according to the amount of missing adhesive, failure at the NCF material either do not initiate or do not accumulate much due to the small loads being developed at the joint.

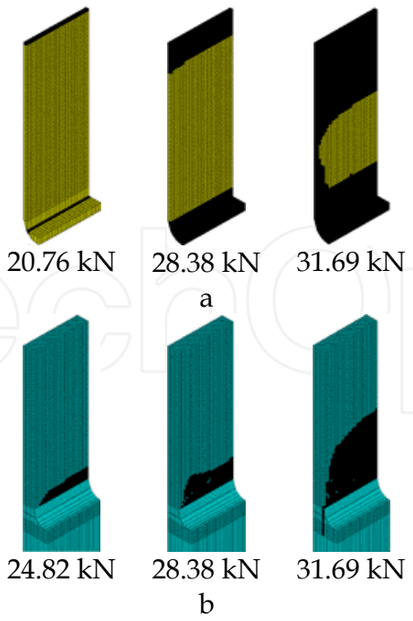

Fig. 20. a. Predicted initiation and progression of debonding (dark area) as a function of pull-out force at the C1 specimen and b. Predicted initiation and progression of matrix cracking as a function of pull-out force at the composite boundary layer of C1 specimen.

7. Adhesively bonded flap-track beam

In the frame of the European Project 'MOJO' (Modular Joints for Composite Aircraft Structures) (MOJO, 2006), a material-driven design for composite modular bonded joints was developed by treating both aspects of adhesive bonding and composites of enhanced through-thickness strength. The outcome of the research is the development of modular NCF Pi(π)-, H-, L- and T-shaped joining elements for adhesively bonded joints. The geometry and material of the elements were optimized with regard to strength of the element itself and the load-carrying capability of the bondline using experimental tests and numerical modeling. As a verification structure and demonstrator of the proposed design concept, the flap-track beam (FTB) of the Airbus A400M, originally made from state-of-the-art metallic materials and assembled exclusively by mechanical fasteners, was selected. For the verification and demonstration purposes, all parts, apart from the fittings, have been replaced by composite NCF parts and specific groups of fasteners have been replaced by adhesively bonded joints based on the developed joining elements. The criterion for the proposed design concept to be successful is for the modified FTB to have the capability of carrying the amount and type of load which the FTB has been originally designed to carry. In (Tserpes et al., 2010), the evaluation of the structural integrity of the FTB, performed by using a complicated experimental program and numerical modeling. In this chapter, the numerical part of the work will be briefly presented.

7.1 The FTB: structure, materials and loading conditions

A schematic representation of the FTB, drawn using the CATIA software, is shown in Fig.21a (D2.3.2, 2008). It consists of NCF panels assembled by mechanical fasteners through

metallic connectors and by adhesive bonds through NCF joining elements. The disassembled FTB, in which the different parts are shown and the joining elements are indicated, is depicted in Fig.21b. The structure is symmetric in the three axes except from the differences at the edges where the boundary conditions are applied. The composite panels are the side and top yellow panels and the bottom gray panel. The remaining parts are metallic. Fasteners have been retained in the metal-composite connections, while adhesive bonds have been adopted in the composite-composite connections.

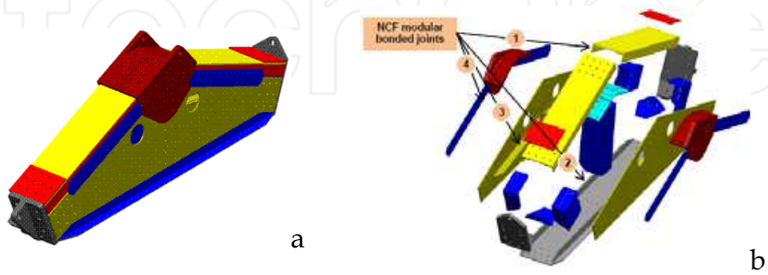

a b

Fig. 21. a. Schematic representation of the FTB drawn with CATIA software (D2.3.2, 2008), and b. the disassembled structure.

The composite panels and joining elements are made of the NCF HTS/RTM6 composite material. The lay-up of the NCF modular joints and panels is quasi-isotropic comprising alterations of the layers except from the L-shapes that are made of layers. The number of layers varies according to panel thickness of the components. Metallic fittings are made either of aluminum or steel. Titanium fasteners have been used for metal-composite junctions and steel ones for metal-metal junctions. For the bonded junctions, the film adhesive Hysol EA9695 and the paste adhesive Hysol 9396 mixed with the 9395 were used. The loading conditions chosen represent realistic distressing situations occurring during service of the FTB. Specifically, the selected load-case corresponds to a landing case of the aircraft at maximum landing weight with applying of full throttle, and with fully deployed flaps but with spoilers retracted. At the left and top edges, the beam is constrained by inserting pins in the holes located there, while in the right corner, loading is applied. An alteration between the static and fatigue load-cases has been adopted in order to examine the fatigue damage tolerance capability of the FTB.

7.2 FE modeling

Complementary and prior to mechanical testing, a 3D detailed FE model of the FTB was built in order to assist design of the experiments, shed light in failure features that cannot be assessed by testing and propose a numerical approach that can be used for the design and analysis of large-scale complicated structural parts. Between the model and experiments, there is a two-way feedback, since the first numerical results aided the design of the experiments, and after the execution of the experiments, the model was improved and validated through the comparison with the experimental results.

The FE model of the FTB was created using the ANSYS FE code. Due to the large number of parts -most of them of complicated geometry- the large number of fasteners and the contact cases, creation of geometry using the ANSYS pre-processor was impossible. To this end, CATIA drawings of the FTB made by SABCA (D2.3.2, 2008) were imported in the ANSYS

ICEM CFD mesh generator as iges files (D2.3.2, 2008). After importing the files, only volumes of the parts, areas and border lines were available for building the mesh. So, in order to build a customized mesh, further modifications had to be made by defining sub-areas and sub-volumes. In order to reduce the total number of elements, specific actions were taken. For instance, a detailed mesh was adopted only in the stress concentration areas and bonded joints and one element was used through the thickness of the parts. The FE mesh of the FTB is shown in Fig.22. All parts of the structure were modelled using the SOLID185 element which is a 8-node structural solid suitable for modeling 3D solid structures. In total, 1,380,000 solid elements were used in the model. Despite that the SOLID185 element has a layered option, it was used as a solid orthotropic element in which the effective properties of the NCF layered material have been assigned. This was done because a layer-wise stress analysis would require an extremely huge computational effort due to the large number of layered elements that should be solved.
The parts of the FTB are assembled by mechanical fasteners and bonded joints. In the model, both joining types have been considered by simulating the exact joining conditions. Fasteners have been modeled as 3D solids consisting of the body and washers following their exact geometry, while bonded joints have been modeled by representing the adhesive with a different single layer of elements.

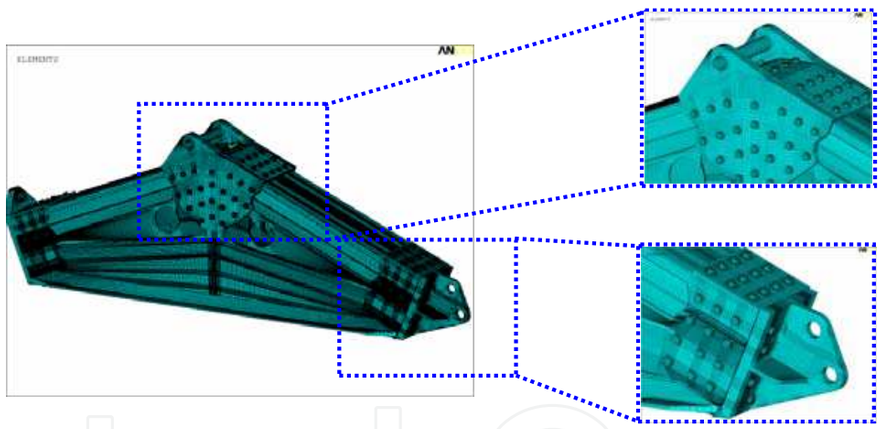

Fig. 22. FE mesh of the FTB.

In the model, all possible contacts between the assembled parts have been considered, namely the surface/surface, the fastener/hole-surface as well as the washer/surface contacts. Contact modeling was done using the ANSYS 3D 4-node surface-to-surface CONTAC173 element. The extremely complicated contact surfaces were generated using the ICEM's feature for automatic generation of contact elements between overlapped areas. The necessary corrections were performed manually afterwards. Almost 272,000 contact elements have been created. Presented in Fig.23 is a close view of the contact elements of the different contact cases. For the friction contacts, a friction coefficient of 0.3 was used. In the model, the exact boundary conditions applied for testing were simulated by creating fully constrained pins inside the holes at the left and top edges of the structure and applying the forces at the internal nodes of the hole at the right edge. As the forces are off-axis with respect to the global coordinate system, they were analyzed into on-axis components.

7.3 PDM

Due to the huge number of composite elements in the model, neither progressive damage modeling in its classical form, comprising the implementation of complicated failure analysis and material property degradation in element basis, nor the mesomechanical approach (Tserpes & Labeas, 2009), which simulates material's behavior based on stiffness-strain functions, could be applied. Therefore, a simplified scheme was adopted for simulating failure in the FTB. A linear material behavior is assumed and each stress component is compared with the corresponding strength (Maximum Stress criterion) and as soon as it exceeds it, the corresponding element stiffness is totally degraded. For the simulation of debonding, the stress intensity at the elements of the adhesive is compared to shear strength.

7.4 Numerical results

7.4.1 Predicted failure initiation

The model has the capability of simulating initiation and progression of the different types of damage in the composite material as well as debonding in the bonded joints. First analyses were conducted prior to the execution of the experiments in order for the predictions of damage initiation to be used for the evaluation of the selected load-cases in the experiments. This was done in order to avoid undesired catastrophic fracture of the specimen.

The predicted failure initiation patterns in the side-panels and bottom panel for the ultimate load are shown in Fig.23. As expected, failure predicted to initiate mainly in the fastener and hole areas due to the stress concentrations. Both tensile and compressive failure modes occurred due to the bending of the structure. The same failure modes have been also predicted in all composite parts connected by the mechanical fasteners. Predicted also is delamination in tension and compression at the edges of all NCF profiles at load levels starting at J=0.22 of the It is important to notice that the aforementioned failures are localized. Regarding bonded joints, it has been found to be whole since no extensive debonding has been predicted by the model. Contrary to the model, in the actual structure, some debonded areas have been detected using ultrasonic inspection after completion of loading (D7.1.1, 2009). These areas are mainly located in the junctions between the H profiles, the top and side panels and they have been resulted by the spreading of initial imperfect bonded areas created in the manufacturing phase. In any case, the bonded joints retain the minimum required integrity. These debonds were not captured by the model because perfect bonding has been assumed in the simulations.

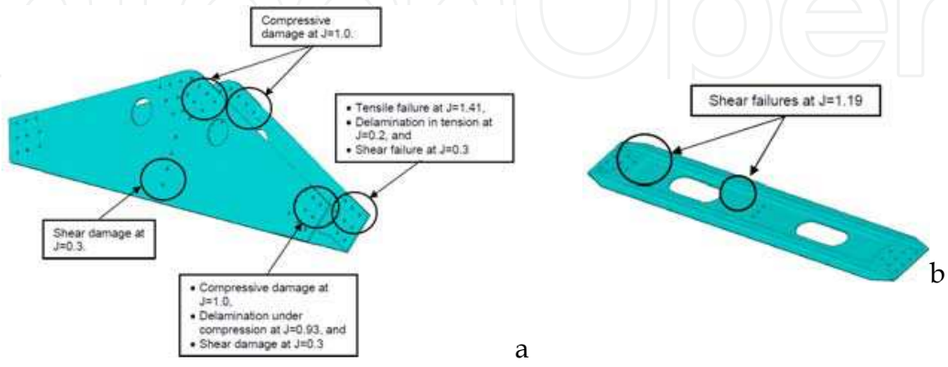

Fig. 23. a. Predicted failure initiation pattern at a. the side-panels, and b. the bottom panel (J=1.0 corresponds to the total amount of the applied load).

7.4.2 Comparison between measured and predicted strain field

In order to monitor the overall behavior of the FTB, a network of 50 strain gauges were mounted on its body. Some of the strain gauges were placed in critical areas with stress concentration (fastener areas and geometrically complex areas) and bonded areas. The measured and computed (nodal) strains for these locations are compared in Table 3. In general, a good agreement is obtained considering the uncertainties in the experimental procedure and the increased numerical errors. The average deviation between two methods is 29.15%. However, in most locations the deviation is lower than 15%. The average deviation is raised by few values exceeding 20%. These values refer to measurement points located inside fastener areas where the strain field is complicated and changes from tension to compression occurs in a very small distance.

The main conclusion from the study on the structural integrity of the novel FTB is that it is capable to effectively transfer the load which the original metallic fastened FTB has been designed to carry, thus validating the proposed design-concept. Localized failures having no significant effect on the integrity of the structure have been detected at fastener areas and bonded joints containing initial defects.

Strain gauge	**Experiment [μstrain]**	**Model [μstrain]**	**Deviation [%]**
1	2282.57	1978	13.3
2	1099.11	996	9.38
5	-262.51	-211	19.62
6	1366.24	1300	4.85
7	-308.23	-354	-14.85
8	-769.23	-701	8.87
9	-1016.07	-975	4.04
10	-575.09	-541	5.93
11	-411.51	-401	2.56
12	348.91	297	14.88
13	251.16	231	8.03
14	239.12	218	8.83
15	171.65	167	2.71
20	1098.15	821	25.24

Table 3. Comparison between measured and predicted strains of the FTB.

8. Conclusions

In this chapter, the scale-independent capability of the PDM method in predicting the strength of composite materials and structures is demonstrated by presenting the application of the method in 4 structural problems lying from nano- to macro-scale. Specifically, after a short historical overview and an introduction to the PDM method, the applications of the method for predicting tensile strength of pristine and defected CNTs lying in the nano-scale, the tensile response of plain weave composites lying in the micro-scale, the effect of imperfect bonding on the tensile strength of DLS joints lying in the macro-scale and the structural integrity of a novel FTB lying in the large-scale are described. In all cases, the method's predictions have been validated against numerical and experimental

results. The following specific conclusions referring to progress made in the development of the method through these applications are drawn:

- Application to CNTs was the first attempt to use PDM method in the nano-scale. The attempt can be rated as successful since the simulated results have been validated successfully against established molecular mechanics methods. Furthermore, the PDM method gave the opportunity to combine the effectiveness of the FE method with the accuracy of the Morse interatomic potential, thus creating a method having significant advantages over classical molecular methods.
- Application of the PDM method to textile composites by means of multi-scaling and homogenization allows for the transfer of material's mechanical response from micro- to macro-scale. Note that without the consideration of PDM modeling, only the elastic properties of such complex materials can be evaluated.
- Application to the large-scale FTB confirms that such models can be proved very helpful to the design of composite structures through virtual experimentation.

9. References

Belytschko, T., Xiao, S.P., Schatz, G.C. & Ruoff, R.S. (2002). Atomistic simulations of nanotube fracture. *Physical Review B,* 65, 235430.

D2.3.2 MOJO Deliverable by SABCA (2008). Final drawing set of A and B level components.

D7.1.1 MOJO Deliverable by EADS-IWF (2009). NDT parameters and industrial NDT for MOJO.

Iijima, S. (1991). Helical microtubules of graphitics carbon. Nature, 354, 56-8.

Kachanov, M.L. (1958). On the creep fracture time. *Izv. Akad. Nauk. SSR.* 8, 26-31.

Llopart P. Ll., Tserpes, K.I., Labeas, G.N. (2010). Experimental and theoretical investigation of the influence of imperfect bonding on the strength of NCF double-lap shears joints. *Composite Structures,* 92, 1673-1682.

Matzenmiller, A. Lublinear, J. & Taylor, R.L. (1995). A constitutive model for anisotropic damage in fiber-composites. *Mechanics of Materials,* 20, 125–152.

Mielke, S.L., Troya, D., Zhang, S., Li, J-L., Xiao, S., Car, R., Ruoff, R.S., Schatz, G.C. & Belytschko, T. (2004). The role of vacancy defects and holes in the fracture of carbon nanotubes. *Chemical Physics Letters*, 390, 413-420.

Modular Joints for Aircraft Components (MOJO) (2006). Research Project funded by the European Commission within the frame of 6th Framework-Aeronautics and Space. Description of Work.

Qian, D., Dickey, E.C., Andrews, R. & Rantell, T. (2000). Load transfer and deformation mechanisms in carbon nanotube-polystyrene composites. *Applied Physics Letters*, 76(20), 2868-2870.

Tang, X. & Whitcomb, J.D. (2003). Progressive Failure Behaviors of 2D Woven Composites, *Journal of Composite Materials,* 37, 1239-1259.

Tserpes, K.I, & Labeas, G.N. (2009). Mesomechanical analysis of non-crimp fabric composite structural parts. *Composite Structures,* 87, 358-369.

Xiao, J.R., Gama, B.A. & Gillespie Jr., J.W. (2007). Progressive damage and delamination in plain weave S-2 glass/SC-15 composites under quasi-static punch-shear loading. *Composite Structures,* 78, 182-196.

Verpoest, I. Lomov, S.V. (2005). Virtual textile composites software WiseTex: Integration with micro-mechanical, permeability and structural analysis.
Composites Science and Technology, 65, 2563-2574.

Yu, M.F., Lourie, O., Dyer, M.J., Moloni, K., Kelly, T.F. & Ruoff, R.S. (2000). Strength and breaking mechanism of multiwalled carbon nanotubes under tensile load. *Science*, 287, 637.

Yokozeki, T., Iwahori, Y. & Ishiwata, S. (2007). Matrix cracking behaviors in carbon fiber/epoxy laminates filled with cup-stacked carbon nanotubes (CSCNTs), *Composites Part A*, 38, 917-924.

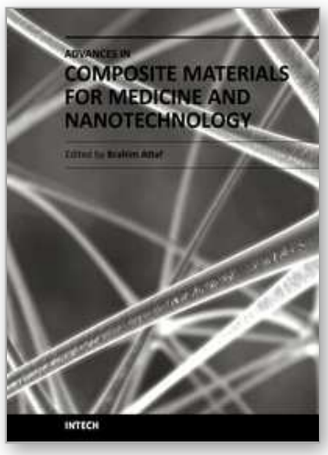

Advances in Composite Materials for Medicine and Nanotechnology

Edited by Dr. Brahim Attaf

ISBN 978-953-307-235-7
Hard cover, 648 pages
Publisher InTech
Published online 01, April, 2011
Published in print edition April, 2011

Due to their good mechanical characteristics in terms of stiffness and strength coupled with mass-saving advantage and other attractive physico-chemical properties, composite materials are successfully used in medicine and nanotechnology fields. To this end, the chapters composing the book have been divided into the following sections: medicine, dental and pharmaceutical applications; nanocomposites for energy efficiency; characterization and fabrication, all of which provide an invaluable overview of this fascinating subject area. The book presents, in addition, some studies carried out in orthopedic and stomatological applications and others aiming to design and produce new devices using the latest advances in nanotechnology. This wide variety of theoretical, numerical and experimental results can help specialists involved in these disciplines to enhance competitiveness and innovation.

InTech Europe
University Campus STeP Ri
Slavka Krautzeka 83/A
51000 Rijeka, Croatia
Phone: +385 (51) 770 447
Fax: +385 (51) 686 166
www.intechopen.com

InTech China
Unit 405, Office Block, Hotel Equatorial Shanghai
No.65, Yan An Road (West), Shanghai, 200040, China
中国上海市延安西路65号上海国际贵都大饭店办公楼405单元
Phone: +86-21-62489820
Fax: +86-21-62489821

IntechOpen